Methylphosphonic Acid Detection using DNA Aptamer-Citrate Capped Gold Nanoparticles Enhanced by Digital Image Analysis

Fellyzra Elvya Pojol[1], Nur Athirah Zulkifli[2], Keat Khim Ong[2,3*], Mohd Junaedy Osman[3], Jahwarhar Izuan Abd Rashid[3], Wan Md Zin Wan Yunus[4,5], Siti Hasnawati Jamal[3], Syed Mohd Shafiq Syed Ahmad[3] and Chin Chuang Teoh[6]

[1]Department of Defence Science, Faculty of Defence Science and Technology, Universiti Pertahanan Nasional Malaysia, Kem Sungai Besi, 57000 Kuala Lumpur, Malaysia

[2]Research Centre for Chemical Defence, Universiti Pertahanan Nasional Malaysia, Kem Sungai Besi, 57000 Kuala Lumpur, Malaysia

[3]Department of Chemistry and Biology, Centre for Defence Foundation Studies, Universiti Pertahanan Nasional Malaysia, Kem Sungai Besi, 57000 Kuala Lumpur, Malaysia

[4]Centre for Tropicalisation, Universiti Pertahanan Nasional Malaysia, Kem Sungai Besi, 57000 Kuala Lumpur, Malaysia

[5]Faculty of Defence Science and Technology, Universiti Pertahanan Nasional Malaysia, Sungai Besi Camp, 57000, Kuala Lumpur, Malaysia

[6]Engineering Research Centre, MARDI, Headquarters Serdang, 43400 Serdang, Selangor, Malaysia

*Corresponding author (e-mail: ongkhim@upnm.edu.my)

Methylphoshonic acid (MPA) is a metabolite of several organophosphorus (OP) nerve agents. The aim of this study was to optimise MPA detection by gold nanoparticles capped with DNA aptamer-citrate using a centred central composite design response surface methodology. The independent variables investigated included the concentration of citrate-capped gold nanoparticles (cit-AuNPs) (A), concentration of DNA aptamer (D), and the incubation period (P) for binding the cit-AuNPs to the DNA aptamer. Analysis of variance (ANOVA) was used to determine the significance of the variables and the interactions between them. A second-order polynomial model was developed to predict the detection response (ΔRGB value). The results demonstrated that A, D, P, A^2, D^2, P^2, AP, and DP were factors that significantly affected ΔRGB values at a 95% confidence level. Good correlations between the experimental and predicted values were supported by the high F-value (721.09), very low p-value (<0.0001), non-significant lack of fit, and a high coefficient of determination (R^2 = 0.9944). The optimum concentration of cit-AuNPs, concentration of DNA aptamer, and incubation period for binding cit-AuNPs to the DNA aptamer were found to be 0.34 nM, 3.9 µM, and 18 min, respectively. A practical application of this sensor is as an environmental monitoring tool for on-site detection of MPA.

Key words: Colorimetric; DNA aptamer; gold nanoparticles; methylphosphonic acid; RGB

Received: October 2021; Accepted: July 2022

Chemical warfare agents (CWAs) are extremely toxic synthetic chemicals that can be dispersed as gases, liquids or aerosols or as agents adsorbed to particles to form a powder. These CWAs have either lethal or incapacitating effects on humans [1]. Among the chemical warfare agents, the nerve agents (NAs) are particularly hazardous. These cause rapid and severe health effects by blocking the function of acetylcholinesterase, an enzyme that is vital to the central nervous system [2-4]. NAs are a subcategory of organophosphorus (OP) compounds, and they have been used in wars and terrorist activities [5]. They decompose rapidly with water via hydrolysis to yield corresponding alkyl phosphonic acids, phosphonothioic acids and various alkyl amino ethanol compounds when NAs are exposed to the environment [6-7], and these eventually degrade to methylphosphonic acid (MPA) via hydrolysis [7]. MPA is resistant to photolysis, hydrolysis, and biodegradation because the bond formed between carbon and phosphorus in the MPA molecule cannot be cleaved or metabolized by plants or animals; thus MPA is a stable hydrolysis product [8]. Thus, the degradation products of NAs can be an indicator of NAs in the environment and may play a key role in assessing the degree of parent agent contamination [9]. Portable and rapid field detection of NA hydrolysis products is desirable for screening purposes and to augment standard laboratory methods [10].

Sensitive and selective colorimetric sensors have been widely adopted as they are simple, rapid, precise and use common laboratory instruments [11]. Colorimetric biosensors can detect a particular analyte based on colour changes easily seen by the naked eye or by using simple portable optical detectors for quantitative measurement [12]. Indeed, the accuracy of the colorimetric method by the naked eye can be

increased using digital image analysis. In a previous study, a digital image-based method using an office scanner was utilized to determine OPs in food samples [13]. Later, Fu *et al.* [14] developed a smartphone-based colorimetric dipstick reader for rapid monitoring of OPs. A digital image-based method was utilized in the determination of organophosphates and carbamates [15]. Image analysis has also been applied to enhance the accuracy of acephate detection [16]. In addition, the colorimetric biosensor may be modified using either nanoparticles or biological recognition or both [17]. Gold nanoparticles (AuNPs) are extensively used in colorimetric sensing due to their simplicity, cost-effective fabrication, and ease of use [18-19]. Aptamers are single-stranded oligonucleotides (DNA or RNA) that form stable and specific complexes with the target molecules by changing conformation [20-22], and have been used to enhance the selectivity of sensors. For example, the synergistic molecular assembly of aptamers on AuNPs was also reported by Abnous *et al.* [23] for the selective and sensitive colorimetric detection of malathion in spiked human serum samples. Moreover, Mondal *et al.* [24] conjugated AuNPs with aptamers, which resulted in the aggregation of AuNPs, and the colour of the AuNP solution changed from red to blue/violet. Furthermore, Liu *et al.* [25] developed a colorimetric detection method based on broad-spectrum aptamers on AuNPs for specific recognition of isocarbophos and omethoate. However, to the best of our knowledge, there is little research on colorimetric biosensors for detecting NA degradation products.

The main objective of this study was to develop DNA aptamer-cit-AuNPs for the detection of MPA, with detection accuracy enhanced by digital image analysis. To achieve this objective, optimisation of detection conditions (including concentration of cit-AuNPs, the concentration of DNA aptamer, and the incubation period for binding cit-AuNPs with DNA aptamer) was performed using response surface methodology (RSM) based on a face-centred central composite design (FCCCD).

EXPERIMENTAL

1. Materials

Gold (III) chloride trihydrate ($HAuCl_4.3H_2O$) was purchased from Sigma (USA). Trisodium citrate dihydrate ($C_6H_5Na_3O_7.2H_2O$) and methylphosphonic acid ($CH_3P(O)(OH)_2$) were purchased from Merck (Germany) and used without further purification. Thiolated DNA aptamer (5'-/5ThiolMC6-D/ATC CGT CAC ACC TGC TCT CGA TGA GAC AAG AGG AAC ACG GCA CAA TTG ATT TAA TGG TGT TGG CTC CCG TAT-3') [26] and IDTE buffer pH 8.0 (IXTE solution) were purchased from Integrated DNA Technologies (Singapore).

2. Preparation of Solutions

2.1. Gold (III) Chloride Trihydrate and Trisodium Citrate Dihydrate Solutions

Briefly, 100 mL solutions each containing 0.2157 mM of gold (III) chloride trihydrate ($HAuCl_4.3H_2O$) and 34 mM trisodium citrate dihydrate were prepared using MilliQ water (18.2 MΩ.cm, Milli-Q, Millipore) in different volumetric flasks.

2.2. Methylphosphonic Acid Stock and Working Solutions

A stock solution of 50 mM methylphosphonic acid (MPA) was prepared by dissolving the desired amount of MPA with MilliQ water in a volumetric flask. This was then stored at 4 °C for further use. MPA working standard solutions were freshly prepared by serial dilution of the MPA stock solution with MilliQ water.

2.3. DNA Aptamer Stock and Working Solutions

A stock solution of DNA aptamer (100 µM) was prepared by dissolving the DNA aptamer with 828 µL IDTE buffer solution. For the detection of MPA, DNA aptamer working solutions were freshly prepared by dilution.

3. Synthesis of Citrate-capped Gold Nanoparticles (cit-AuNPs)

Unmodified cit-AuNPs were synthesised according to Turkevich *et al.* [27] by reduction of tetrachloroauric acid ($HAuCl_4$) by trisodium citrate solution. Gold (III) chloride trihydrate solution (100 mL, 0.2157 mM) was boiled to 100 °C in a 250 mL conical flask while stirring at 1,500 rpm for 15 min. Then, 2 mL of 34 mM trisodium citrate solution was added to the gold (III) chloride trihydrate solution under vigorous stirring. The solution eventually changed from pale yellow to a light red wine, indicating the formation of cit-AuNPs. The solution was allowed to cool to room temperature, and then centrifuged at 12,000 rpm for 30 min to remove excess trisodium citrate. The precipitate (concentrated cit-AuNPs) was collected and stored at 4 °C for further use. A schematic diagram of the synthesis is shown in Figure 1.

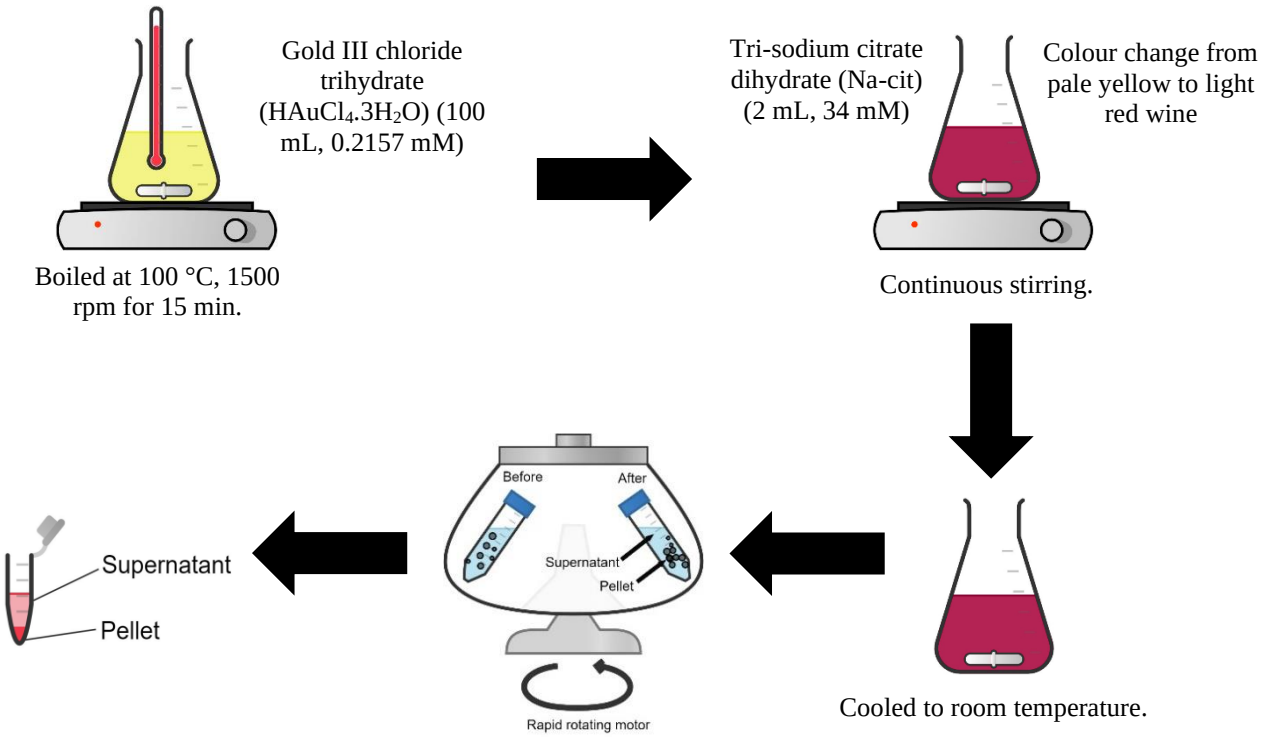

Figure 1. Schematic diagram of citrate-capped gold nanoparticles (cit-AuNPs) synthesis (created with Chemix) (https://chemix.org).

The synthesised cit-AuNPs had a concentration of 0.538 nM, according to the calculation proposed by Zuber *et al*. [28].

$$C_{AuNPs} = 6\left(\frac{C_{Au} * M_{Au}}{\pi * \rho_{Au} * {D_{AuNPs}}^3 * N_A}\right)$$

where C_{AuNPs} is the molar concentration of the cit-AuNPs (M), C_{Au} is the molar concentration of the gold atoms/ions (M), M_{Au} is the molecular weight of gold ($gmol^{-1}$), ρ_{Au} is the density of gold (19.3 $g.cm^{-3}$), D_{AuNPs} is the diameter of the cit-AuNPs and N_A is the Avogadro constant (mol^{-1}). The mean diameter of the cit-AuNPs synthesised in this study (23.5 nm) was determined from our previous study [29].

3.1. Characterisation of cit-AuNPs

3.1.1. Fourier transform infrared (FTIR) spectroscopy

FTIR spectra were recorded on a Perkin Elmer Frontier spectrophotometer. One microlitre of the centrifuged AuNPs was placed on the diamond crystal plate. Infrared spectra of the sample were recorded in the region of 400-4000 cm^{-1}.

3.1.2. Ultraviolet-visible (UV-vis) spectrometry

The UV-vis spectrum of the centrifuged AuNPs was recorded on a UV-3600i Plus UV-Vis-NIR spectrophotometer (Shimadzu, Japan) at a wavelength range of 300 to 900 nm.

3.2. Experimental design

In this study, the response surface methodology (RSM) method based on the face-centred central composite design (FCCCD) was used to design the experiment and optimise the DNA aptamer/cit-AuNPs colorimetric assay using Minitab 17 software. The optimisation involved the following three factors: concentration of the cit-AuNPs (A), concentration of the DNA aptamer (D), and incubation period for binding the cit-AuNPs with the DNA aptamer (P), at their low, centre, and high levels as presented in Table 1. The experimental design required 20 experimental runs to optimise the factors with 8 factorial points, 6 centre points in cube, and 6 axial points (Table 2).

Table 1. Independent variables and their levels used for MPA detection by DNA aptamer/cit-AuNPs.

Symbol	Factor	Unit	Low level (-1)	Centre level (0)	High level (+1)
A	Concentration of cit-AuNPs	nM	0.27	0.35	0.43
D	Concentration of DNA aptamer	µM	1	5	9
P	Incubation period for binding cit-AuNPs with DNA aptamer	min	0	30	60

Table 2. Design matrix of the independent variables investigated in this study.

Run order	Concentration of cit-AuNPs (nM)	Concentration of DNA aptamer (µM)	Incubation period for binding cit-AuNPs with DNA aptamer (min)
1	0.35	5	30
2	0.27	9	0
3	0.35	5	30
4	0.27	1	0
5	0.43	9	0
6	0.35	5	30
7	0.27	9	60
8	0.35	5	30
9	0.35	5	60
10	0.43	9	60
11	0.35	5	30
12	0.35	9	30
13	0.27	5	30
14	0.35	5	30
15	0.27	1	60
16	0.43	1	0
17	0.35	5	0
18	0.43	5	30
19	0.35	1	30
20	0.43	1	60

The experimental design was evaluated with a second-order polynomial model using multiple linear regression based on equation (1):

$$Y = \beta_o + \sum \beta_i X_i + \sum \beta_{ij} X_i X_j + \sum \beta_{ii} X_i^2 \qquad (1)$$

where Y is the predicted response (ΔRGB), β_o is the intercept, β_i is the effect of the linear term, β_{ii} is the effect of the quadratic term, β_{ij} is the effect of the interaction term, and X_i is the coded value of the corresponding i^{th} factor.

The significance, adequacy, and validity of the model were evaluated by analysis of variance (ANOVA), and a p-value of less than 0.05 indicated significance at a 95% confidence level. Three-

dimensional (3D) surface plots were used to visualize the interactive effects between two independent variables and the response [30]. Minitab 17 response optimiser was used to determine the optimum conditions for the colorimetric assay.

3.3. Colorimetric detection of MPA

A desirable volume of cit-AuNPs was mixed with 1 µL of DNA aptamer in a 3 mL screw-cap glass vial and incubated at 37 °C for a certain period (Table 2). Subsequently, MPA was added into the vial until the solution reached a total volume of 1 mL, and then the mixture was swirled. After 20 seconds, the colour of the solution was captured using a smartphone that was placed at a distance of 9 cm from the sample in an image capturing box. The experiments were conducted at room temperature.

3.4. Image processing of the captured images

The captured images of the solutions were analysed using an ImageJ software to obtain digital red (R), green (G) and blue (B) values. At first, the captured image of the solution from above was analysed using the "oval" tool in the software to highlight the desired area and to remove the background lighting effect. The R, G, and B values were then measured and used to calculate the response (ΔRGB) by subtracting the colour intensity of the blank and sample using Equation 2 [31].

$$\Delta\text{RGB} = \sqrt{(R_0 - R_1)^2 + (G_0 - G_1)^2 + (B_0 - B_1)^2} \quad (2)$$

where R_o, G_o, and B_o are red, green, and blue values for the blank, while R_1, G_1, and B_1 are red, green, and blue values for MPA, respectively.

RESULTS AND DISCUSSION

1. Characterisations of cit-AuNPs

The cit-AuNPs were synthesised based on the chemical reduction of gold ions (Au^{3+}) to gold atoms (Au^0) using trisodium citrate. In this study, the centrifuged cit-AuNPs were characterised by FTIR and UV-vis spectroscopy.

1.1. FTIR spectroscopy

Attenuated total reflectance-Fourier transform infrared spectroscopy (ATR-FTIR) measurements were conducted on the trisodium citrate dihydrate and cit-AuNPs samples to confirm the formation of cit-AuNPs, and the resulting spectra are shown in Figure 2. The characteristic band for citrate can be observed in the spectrum of trisodium citrate at 1580 cm^{-1} which is assigned to carboxylate (COO^-) asymmetric stretching, as shown in Figure 2a. Other peaks at 1278 cm^{-1} and 1078 cm^{-1} are due to C-O stretching (C-O S). In addition, a small peak at 610 cm^{-1} represents carboxylate bending (COO^- bending).

In the FTIR spectrum of cit-AuNPs (Figure 2b), a broad band above 3000 cm^{-1} suggests O-H stretching and indicates the presence of water molecules. These peaks are related to the interaction of water with the free carboxylic acid groups of the adsorbed citrate anions on the nanoparticles, and the high intensity of this absorption band is due to hydrogen-bonding arising from the (−COOH H_2O ··HOOC−) intermolecular interaction [32]. It is well-known that carboxylic acid molecules with no other polar groups usually exist predominantly as the hydrogen-bonded dimer, which results in a very broad OH stretching band around 3000 cm-^{1} [33]. A sharp peak at 1638 cm^{-1} can be assigned to COO^- asymmetric stretching. When comparing the peaks for COO^- asymmetric stretching in both spectra, it was observed that the COO^- asymmetric stretching peak in the cit-AuNPs spectrum had shifted to a higher wavenumber, indicating that the binding of cit-AuNPs had occurred through unidentate coordination of citrate ions anchoring only one oxygen atom [34–36]. Similar results were reported by Osman *et al.* [36]. There was also a noticeable broad band at 546 cm^{-1} which may be due to COO^- bending. These results confirmed the presence of citrate anions in the synthesised cit-AuNPs.

1.2. UV-vis Spectroscopy

Gold nanoparticles exhibit a distinct optical feature commonly referred to as localized surface plasmon resonance (LSPR), which is the collective oscillation of electrons in the conduction band of AuNPs in resonance with a specific wavelength of incident light. LSPR of AuNPs result in a strong absorbance band in the visible region (500 nm-600 nm), which can be measured by UV-vis spectroscopy. Figure 3 shows the absorbance spectrum of the synthesised cit-AuNPs, where the LSPR peak was observed at around 520 nm. The presence of the LSPR peak indicates the successful synthesis of AuNPs from the reduction of Au^{3+} of $HAuCl_4.3H_2O$ solution. Jiang *et al.* [37] attributed this peak to the transverse ligand mode (in-phase) of the induced dipole. In addition, Gosh and Pal [38] suggested that the transverse mode showed a resonance coinciding with the plasmon band of spherical particles, e.g., at 520 nm. The shape and position of surface plasmon absorption depends on the particle size, its shape and the dielectric constant of the surrounding medium [39–40]. Obviously, a sharp peak found in the spectrum (Figure 3) indicates a uniform particle size [41].

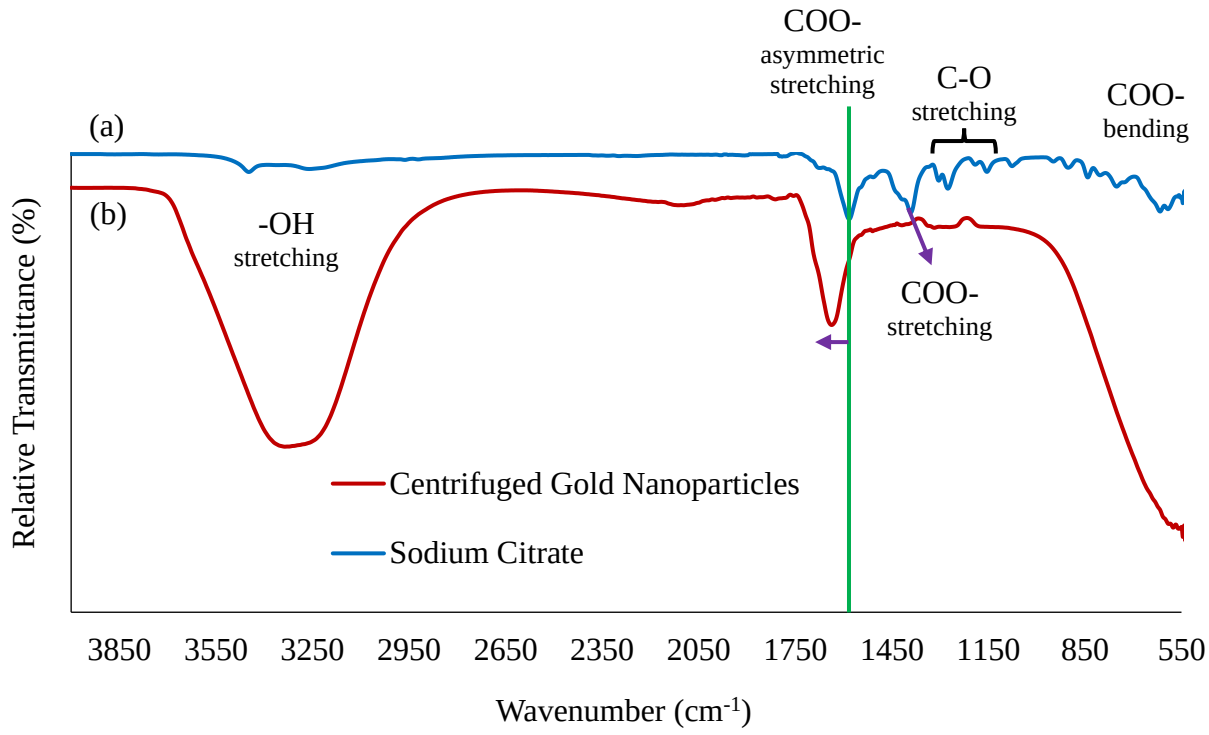

Figure 2. FTIR spectra of (a) trisodium citrate and (b) centrifuged AuNPs.

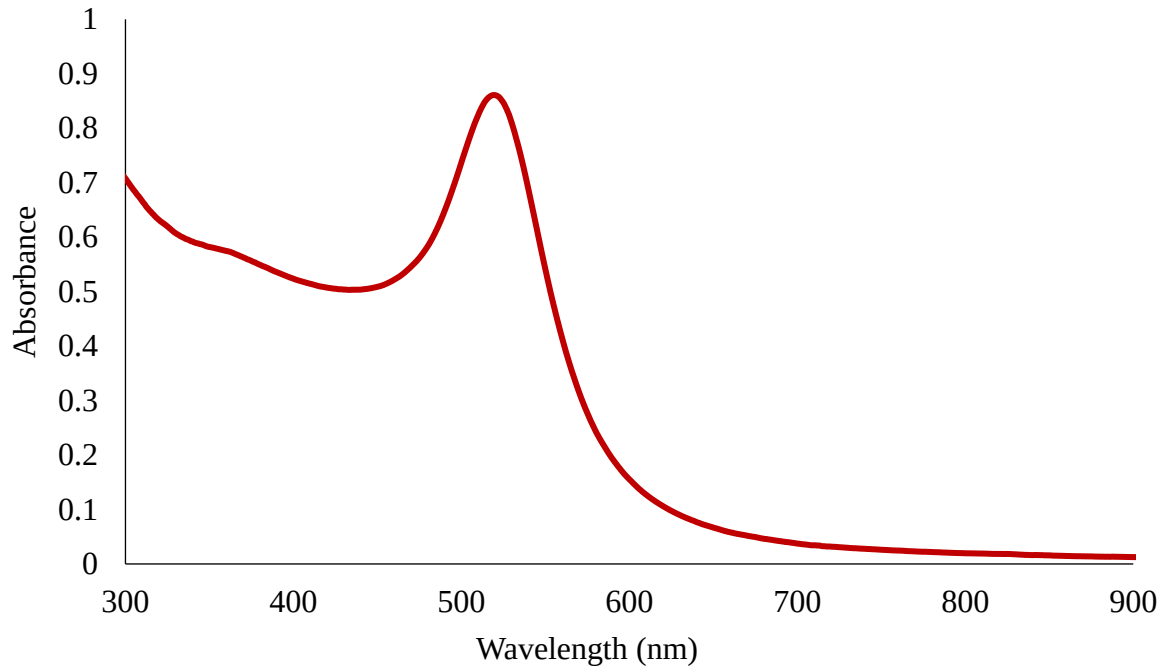

Figure 3. Absorption spectrum of the synthesised cit-AuNPs

2. Experimental Design and Statistical Analysis

In this study, FCCCD based on RSM was used to determine the influence of certain factors (concentration of cit-AuNPs, concentration of DNA aptamer, and incubation period for binding cit-AuNPs with DNA aptamer) on the colorimetric assay. A set of 20 experimental runs was conducted, and the results of the experimental responses were compared with the predicted responses (Table 3). Higher experimental and predicted responses (ΔRGB) were obtained in the current study as compared to our previous study [42] where cit-AuNPs were synthesised using an "inverse" cit-AuNPs synthesis method and used in the detection of MPA.

Table 3. Response surface design using FCCCD and the experimental and predicted responses.

Run	Concentration of cit-AuNPs (nM)	Concentration of DNA aptamer (μM)	Incubation period for binding cit-AuNPs with DNA aptamer (min)	Response, ΔRGB	
				Experimental	Predicted
1	0.35	5	30	48	47
2	0.27	9	0	32	32
3	0.35	5	30	48	47
4	0.27	1	0	35	35
5	0.43	9	0	24	24
6	0.35	5	30	47	47
7	0.27	9	60	29	29
8	0.35	5	30	48	47
9	0.35	5	60	43	44
10	0.43	9	60	23	23
11	0.35	5	30	47	47
12	0.35	9	30	44	44
13	0.27	5	30	36	36
14	0.35	5	30	47	47
15	0.27	1	60	30	30
16	0.43	1	0	27	27
17	0.35	5	0	47	47
18	0.43	5	30	28	29
19	0.35	1	30	46	46
20	0.43	1	60	24	24

Table 4. Analysis of variance (ANOVA) of the response surface quadratic model for predicting ΔRGB.

Source	Sum of squares	DF	Mean square	F-value	*p*-value	
Model	1775.81	9	197.313	721.09	0.000	Significant
A	129.20	1	129.600	473.62	0.000	
D	10.00	1	10.000	36.54	0.000	
P	25.60	1	25.600	93.55	0.000	
A^2	1566.45	1	630.051	2302.51	0.000	
D^2	27.61	1	12.551	45.87	0.000	
P^2	12.55	1	12.551	45.87	0.000	
AD	0.00	1	0.000	0.00	1.000	
AP	2.00	1	2.000	7.31	0.022	
DP	2.00	1	2.000	7.31	0.022	
Residual	2.74	10	0.274			
Lack of fit	1.24	5	0.274	0.82	0.581	Not significant
Pure error	1.50	5	0.300			
Cor total	1778.55	19				

$R^2 = 0.9944$; $R^2_{predicted} = 0.9985$; $R^2_{adjusted} = 0.9971$

Table 5. Estimated regression coefficients, *t*-values, and *p*-values.

Terms	Effects	Coefficients	SE Coefficient	*t*-value	*p*-value
Constant		47.36	0.18	263.33	0.00
A	-7.20	-3.60	0.17	-21.76	0.00
D	-2.00	-1.00	0.17	-6.05	0.00
P	-3.20	-1.60	0.17	-9.67	0.00
A^2	-30.27	-15.14	0.32	-47.98	0.00
D^2	-4.27	-2.14	0.32	-6.77	0.00
P^2	-4.27	-2.14	0.32	-6.77	0.00
AD	-0.00	-0.00	0.19	-0.00	1.00
AP	1.00	0.50	0.19	2.70	0.02
DP	1.00	0.50	0.19	2.70	0.02

Analysis of variance (ANOVA) was performed to evaluate the significance of the overall model and each regression coefficient. The results revealed high conformity between the experimental (ΔRGB) and predicted responses. The ANOVA shows the linear terms, the squared terms, and the interactions between the factors (Table 4).

The *p*-value of the model was 0.000 and the obtained F-value was 721.09, which is higher than the F-critical value ($F_{0.05,9,10}$ = 3.02), implying that the model was significant at a 95% confidence level. This indicates that the experimental data obtained fitted well with the model. Moreover, the lack of fit (F-value=0.82) was insignificant (*p*-value > 0.05) relative to the pure error which indicates that the quadratic model was statistically significant for the response, thus it can be used for further analysis. In addition, the fit of the models was evaluated by the determination of coefficients (R^2) and adjusted R^2 (R^2_{adjusted}) [43].

The R^2 value should be close to 1 for the model to fit the experimental data. According to the ANOVA results (Table 4), the high R^2 (0.9944) and adjusted R^2 (0.9971) values were very close, indicating that the model was able to predict the response accurately. Also, the predicted *R*-squared ($R^2_{\text{predicted}}$) was 0.9985, which is in good agreement with the actual R^2_{adjusted} (0.9971). Overall, the ANOVA results showed that the proposed model can be used to navigate the design space. To evaluate the significance of each term of the model, a *p*-value was used. Model terms with *p*-values ≤ 0.05 were considered significant, and terms with *p*-values > 0.05 were regarded as insignificant. The results demonstrated that the concentration of cit-AuNPs (A), concentration of DNA aptamer (D), and the incubation period for binding cit-AuNPs with DNA aptamer (P), A^2, D^2, P^2, AP, and DP were significant factors affecting ΔRGB values as indicated by the *p*-values ≤ 0.05. The estimated regression coefficients, *t*-value, and *p*-value for the linear, quadratic and interaction effects of the variables are presented in Table 5 at a 95% significance level.

The experimental data (ΔRGB) (Table 3) were used in developing the RSM model. The empirical relationship between the actual factors and the response was presented by the following second-order polynomial equation in terms of coded factors:

$$\Delta RGB = 47.36 - 3.60A - 1.00D - 1.60P - 15.14A^2 - 2.14D^2 - 2.14P^2 + 0.50AP + 0.50DP \quad (3)$$

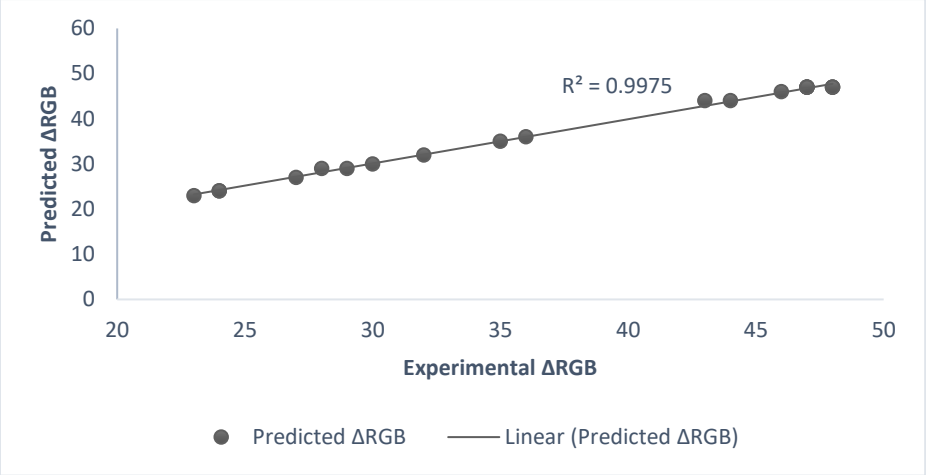

Figure 4. Correlation between experimental and predicted ΔRGB values by FCCCD model.

in which A, D, and P represent the concentration of cit-AuNPs, concentration of DNA aptamer, and the incubation period for binding cit-AuNPs with the DNA aptamer, respectively.

The coefficient values and signs obtained from the model equation indicate how each factor affected the response [44]. Notably, the positive values of the equation showed positive effects on the response, and vice versa [45-46]. From equation 3, it can be seen that AP and DP presented positive values attributed to the synergistic effect. In contrast, A, D, P, A^2, D^2, and P^2 presented negative values attributed to the antagonistic effect. A, D, and P had coefficients of –3.60, –1.00, and –1.60, respectively, therefore, the highest main effect was due to factor A. The largest interaction effect belonged to AD and DP, both with coefficients of +0.50. The highest square effect belonged to A^2 which had a coefficient of –15.14.

Figure 4 depicts the relationship between the predicted ΔRGB values of the model and the experimental ΔRGB values. A linear distribution plot was observed, with data distributed close to the straight line, indicating a well-fitted model with good prediction ability.

3. Three-dimensional Response Surface Plots

Three-dimensional (3D) response surface plots were used in this study to illustrate the interactions between three factors (concentration of cit-AuNPs, concentration of DNA aptamer, and incubation period for binding cit-AuNPs with DNA aptamer). As illustrated in Figure 5, the effects of two relative factors were tested as one factor was kept constant at the centre level.

Figure 5(a) presents the response surface plot of the concentration of cit-AuNPs (A) and concentration of DNA aptamer (D) on ΔRGB values. As can be seen from this figure, increasing the concentration of cit-AuNPs (A) and the concentration of DNA aptamer (D) to the centre level resulted in an increase in ΔRGB values to a point, then the response decreased steadily. At low DNA aptamer concentrations, there are insufficient binding sites on the DNA aptamer available for the cit-AuNPs. Conversely, an excess amount of DNA aptamer is present at high concentrations, which acts as an electrostatic barrier [47]. However, the maximum ΔRGB was estimated close to the centre level of both factors, implying that the amounts of cit-AuNPs (A) and DNA aptamer were sufficient for the detection of MPA at this level. Plotnikov *et al*. [48] found that the application of AuNPs at high concentrations (0.1 mg/ml and above) caused a noticeable amount of DNA damage.

The effects of the interactive relationship between the concentration of cit-AuNPs and incubation period for binding cit-AuNPs with DNA aptamer (AP) on the response are illustrated in Figure 5(b). The ΔRGB increased with the increasing concentration of cit-AuNPs and incubation time from low to centre level. The ΔRGB value then decreased as the concentration of cit-AuNPs (A) increased with longer incubation periods for binding cit-AuNPs with DNA aptamer (P). This phenomenon might be caused by the disassembly of DNAs due to high cit-AuNPs concentrations and long incubation periods for binding cit-AuNPs with DNA aptamer as reported by Wang *et al*. [49]. Still, this interaction effect significantly influenced the response. In addition, the maximum ΔRGB can be observed near to the centre levels of both factors.

The combined effects of DNA aptamer concentration and incubation period for binding cit-AuNPs with DNA aptamer (DP) on ΔRGB of the developed aptasensor is shown in Figure 5(c). A similar trend was found for this combined effect, where ΔRGB increased with the concentration of DNA aptamer and incubation period from low to centre level, while keeping the concentration of cit-AuNPs at the centre level. Both DNA aptamer

concentration and incubation period substantially affected ΔRGB. However, reduction of ΔRGB was recorded when the concentration of DNA aptamer increased at longer incubation periods. This might be due to the fact that the supercoiled form of DNA decreased with an increased incubation period [50]. Furthermore, an optimal incubation period allows the DNA aptamer to easily bind on the AuNPs surface, which reduces the risk of the sensor giving false positive reactions from non-target analyte molecules [51]. Yet, the highest ΔRGB can be observed at the top of the surface plot (Figure 5c). A previous study reported that the incubation of AuNPs for 24 h resulted in 15-20% DNA damage through the induction of an alkali-labile site, causing single and double strand breaks [52]. Furthermore, a study by Verger *et al*. [53] also showed that the relative amount of supercoiled DNA decreased as the incubation time of plasmid DNA increased from 0 to 25 h.

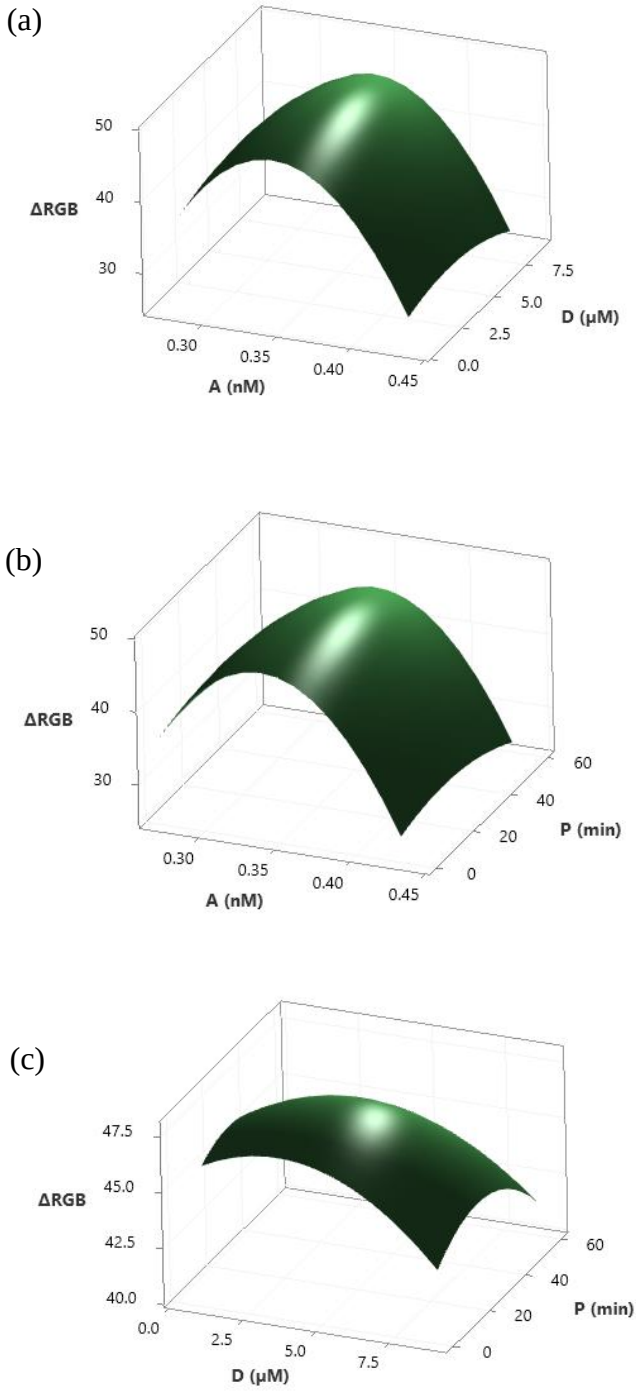

Figure 5. 3D response surface plots for ΔRGB values: (a) interaction between the concentration of cit-AuNPs (A) and the concentration of DNA aptamer (D), (b) interaction between the concentration of AuNPs (A) and incubation period for binding cit-AuNPs with DNA aptamer (P) and (c) interaction between the concentration of DNA aptamer (D) and incubation period for binding cit-AuNPs with DNA aptamer (P).

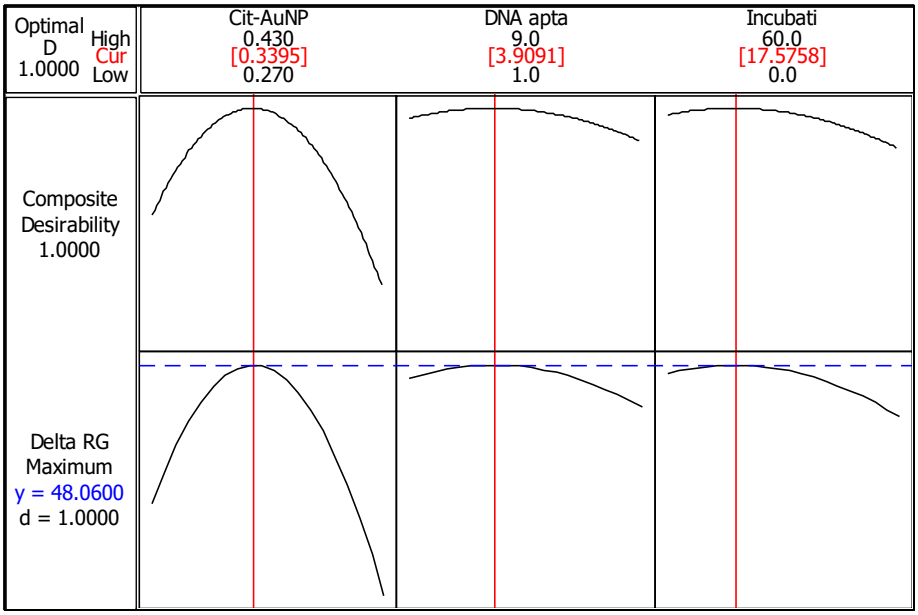

Figure 6. Optimisation plots of the factors affecting ΔRGB value.

4. Optimisation of the Parameters

The optimum values for the concentration of cit-AuNPs, the concentration of DNA aptamer, and the incubation period for binding cit-AuNPs with DNA aptamer were determined by an optimisation plot to obtain the highest response (ΔRGB) using Minitab 17 software. The optimisation plot (Figure 6) shows that the optimised conditions predicted by the RSM model with 1.0000 composite desirability are as follows: 0.34 nM of cit-AuNPs, 3.9 µM of DNA aptamer, and an 18 min incubation period. In contrast, a previous study showed that the optimum conditions to attain the optimum ΔRGB values were 155 nM of cit-AuNPs, 1 µM of DNA and a 24.85 min incubation period [42]. A longer incubation period was required compared to the current study as the DNA concentration was not high enough for the aggregation of aptamer-AuNPs to occur. However, the prolonged incubation period resulted in the partial hybridisation of the aptamers [54].

CONCLUSION

The detection of MPA by DNA aptamer-citrate capped gold nanoparticles was optimised using RSM based on FCCCD. The relationship between the response (ΔRGB) and the independent variables was developed via a quadratic polynomial equation with a high determination coefficient (R^2= 0.9944). The concentration of cit-AuNPs (A), concentration of DNA aptamer (D), and the incubation period for binding cit-AuNPs with DNA aptamer (P), A^2, D^2, P^2, AP, and DP were the significant factors affecting ΔRGB values. The optimum conditions suggested by RSM for attaining maximum ΔRGB values were 0.34 nM of cit-AuNPs, 3.9 µM of DNA aptamer, and an 18 min incubation period for binding cit-AuNPs with DNA aptamer. Qualitative detection by the naked eye without the use of advanced instruments allows rapid on-site detection and makes this method a good tool for environmental monitoring. Furthermore, the proposed biosensing method offers good precision, simplicity and low cost, making it is possible to be used for the detection of MPA in real samples.

ACKNOWLEDGEMENT

This work was financially supported by the Ministry of Higher Education Malaysia through a Fundamental Research Grant Scheme (FRGS/1/2017/STG01/UPNM/02/1). The authors would also like to thank Universiti Pertahanan Nasional Malaysia for providing the research facilities. Also, special thanks to Chemix for the illustration in Figure 1.

REFERENCES

1. Ganesan, K., Raza S. K. and Vijayaraghavan, R. (2010) Chemical warfare agents. *Journal of Pharmacy and Bioallied Sciences*, **2(3)**, 166–178.

2. Burnworth, M., Rowan, S. J. and Weder, C. (2007) Fluorescent sensors for the detection of chemical warfare agents. *Chemistry - A European Journal*, **13(28)**, 7828–7836.

3. Chong, H. and Ching, C. B. (2016) Development of colorimetric-based whole-cell biosensor for organophosphorus compounds by engineering transcription regulator DmpR. *ACS Synthetic Biology*, **5(11)**, 1290–1298.

4. Figueiredo, T. H., Apland, J. P., Braga, M. F. M. and Marini, A. M. (2018) Acute and long-term

consequences of exposure to organophosphate nerve agents in humans. *Epilepsia*, **59**, 92–99.

5. Mukherjee, S. and Gupta, R. D. (2020) Organophosphorus nerve agents: types, toxicity, and treatments. *Journal of Toxicology*, **2020**, 1–16.

6. Steiner, W. E., Harden, C. S., Hong, F., Klopsch, S. J., Hill, H. H. and McHugh, V. M. (2006) Detection of aqueous phase chemical warfare agent degradation products by negative mode ion mobility time-of-flight mass spectrometry [IM (tof)MS]. *Journal of the American Society for Mass Spectrometry*, **17(2)**, 241–245.

7. Otsuka, M., Tsuge, K., Seto, Y., Miyaguchi, H. and Uchiyama, M. (2018) Analysis of degradation products of nerve agents via post-pentafluorobenzylation liquid chromatography-tandem mass spectrometry. *Journal of Chromatography A*, **1577**, 31–37.

8. Baygildiev, T. M., Rodin, I. A., Stavrianidi, A. N., Braun, A. V., Akhmerova, D. I., Shpigun, O. A. and Rybal'chenko, I. V. (2017) Time-efficient LC/MS/MS determination of low concentrations of methylphosphonic acid. *Inorganic Materials*, **53(14)**, 1382–1385.

9. Kubachka, K. M., Richardson, D. D., Heitkemper, D. T. and Caruso, J. A. (2008) Detection of chemical warfare agent degradation products in foods using liquid chromatography coupled to inductively coupled plasma mass spectrometry and electrospray ionization mass spectrometry. *Journal of Chromatography A*, **1202(2)**, 124–131.

10. Che Sulaiman, I. S., Chieng, B. W., Pojol, F. E., Ong, K. K., Abdul Rashid, J. I., Wan Yunus, W. M. Z., Mohd Kasim, N. A., Abdul Halim, N., Mohd Noor, S. A. and Knight, V. F. (2020) A review on analysis methods for nerve agent hydrolysis products. *Forensic Toxicology*, **38(2)**, 297–313.

11. Dai, H., Li, Y., Zhang, Q., Fu, Y. and Li, Y. (2018) A colorimetric biosensor based on enzyme-catalysis-induced production of inorganic nanoparticles for sensitive detection of glucose in white grape wine. *RSC Advances*, **8(59)**, 33960–33967.

12. Zhao, V. X. T., Wong, T. I., Zheng, X. T., Tan, Y. N. and Zhou, X. (2020) Colorimetric biosensors for point-of-care virus detections. *Materials Science for Energy Technologies*, **3**, 237–249.

13. Meng, X., Schultz, C. W., Cui, C., Li, X. and Yu, H. Z. (2015) On-site chip-based colorimetric quantitation of organophosphorus pesticides using an office scanner. *Sensors and Actuators, B: Chemical*, **215,** 577–583.

14. Fu, Q., Zhang, C., Xie, J., Li, Z., Qu, L., Cai, X., Ouyang, H., Song, Y., Du, D., Lin, Y. and Tang, Y. (2019) Ambient light sensor based colorimetric dipstick reader for rapid monitoring organophosphate pesticides on a smart phone. *Analytica Chimica Acta*, **1092(126)**, 126–131.

15. Bordbar, M. M., Nguyen, T. A., Arduini, F. and Bagheri, H. (2020) A paper-based colorimetric sensor array for discrimination and simultaneous determination of organophosphate and carbamate pesticides in tap water, apple juice, and rice. *Microchimica Acta*, **187(11)**, 1–13.

16. Osman, M. J., Yunus Wan, W. M. Z., Ong, K. K., Chieng, B. W., Mohd Kassim, N. A., Mohd Noor, S. A., Knight, V. F., Abdul Rashid, J. I. and Teoh, C. C. (2020) Image digitization of colorimetric detection of acephate based on its complexation with citrate-capped gold nanoparticles. *Journal of Chemistry*, **2020**, 1–10.

17. Diauudin, F. N., Rashid, J. I. A., Knight, V. F., Wan Yunus, W. M. Z., Ong, K. K., Kasim, N. A. M., Abdul Halim, N. and Noor, S. A. M. (2019) A review of current advances in the detection of organophosphorus chemical warfare agents based biosensor approaches. *Sensing and Bio-Sensing Research*, **26**, 1–9.

18. Wei, Q., Nagi, R., Sadeghi, K., Feng, S., Yan, E., Ki, S. J., Caire, R., Tseng, D. and Ozcan, A. (2014) Detection and spatial mapping of mercury contamination in water samples using a smartphone. *ACS Nano*, **8(2)**, 1121–1129.

19. Chang, C. C., Chen, C. P., Wu, T. H., Yang, C. H., Lin, C. W. and Chen, C. Y. (2019) Gold nanoparticle-based colorimetric strategies for chemical and biological sensing applications. *Nanomaterials*, **9(6)**, 1–24.

20. Zhang, J., Liu, B., Liu, H., Zhang, X. and Tan, W. (2013) Aptamer-conjugated gold nanoparticles for bioanalysis. *Nanomedicine*, **8(6)**, 983–993.

21. Tello, A., Cao, R., Marchant, M. J. and Gomez, H. (2016) Conformational changes of enzymes and aptamers immobilized on electrodes. *Bioconjugate Chemistry*, **27(11)**, 2581–2591.

22. Debiais, M., Lelievre, A., Smietana, M. and Müller, S. (2020) Splitting aptamers and nucleic acid enzymes for the development of advanced biosensors. *Nucleic Acids Research*, **48(7)**, 3400–3422.

23. Abnous, K., Danesh, N. M., Ramezani, M., Alibolandi, M., Emrani, A. S., Lavaee, P. and Taghdisi, S. M. (2018) A colorimetric gold nanoparticle aggregation assay for malathion based on target-induced hairpin structure assembly of complementary strands of aptamer. *Microchimica Acta*, **185(4)**, 2–7.

24. Mondal, B., Ramlal, S., Lavu, P. S., Bhavanashri, N. and Kingston, J. (2018) Highly sensitive colorimetric biosensor for staphylococcal enterotoxin B by a label-free aptamer and gold nanoparticles. *Frontiers in Microbiology*, **9**, 1–8.

25. Liu, D. -L., Li, Y., Sun, R., Xu, J. -Y., Chen, Y. and Sun, C. -Y. (2019) Colorimetric detection of organophosphorus pesticides based on the broad-spectrum aptamer. *Journal of Nanoscience and Nanotechnology*, **20(4)**, 2114–2121.

26. Bruno, J. G., Carrillo, M. P., Phillips, T., Vail, N. K. and Hanson, D. (2008) Competitive FRET-aptamer-based detection of methylphosphonic acid, a common nerve agent metabolite. *Journal of Fluorescence*, **18(5)**, 867–876.

27. Turkevich, J., Stevenson, P. C. and Hillier, J. (1951) A study of the nucleation and growth processes in the synthesis of colloidal gold. *Discussions of the Faraday Society*, **11**, 55–75.

28. Zuber, A., Purdey, M., Schartner, E., Forbes, C., Van Der Hoek, B., Giles, D., Abell, A., Monro, T. and Ebendorff-Heidepriem, H. (2016) Detection of gold nanoparticles with different sizes using absorption and fluorescence based method. *Sensors and Actuators, B: Chemical*, **227**, 117–127.

29. Pojol, F. E., Woei, C. B., Khim, O. K., Rashid, A., Izuan, J. and Mohd, O. (2021) Effect of gold nanoparticles size on detection of methyl-phosphonic acid hydrolysis product of nerve agent. *Research Journal of Chemistry and Environment*, **25(7)**, 1–7.

30. Joseph, C. C., Anthony, W. and Anthony, W. (2018) Response surface methodology in application of optimal manufacturing process of axial-flow fans adopted by modern industries. *American Journal of Theoretical and Applied Statistics*, **7(6)**, 235–241.

31. Murdock, R. C., Shen, L., Griffin, D. K., Kelley-Loughnane, N., Papautsky, I. and Hagen, J. A. (2013) Optimization of a paper-based ELISA for a human performance biomarker. *Analytical Chemistry*, **85(23)**, 11634–11642.

32. Boldeiu, A., Simion, M., Mihalache, I., Radoi, A., Banu, M., Varasteanu, P., Nadejde, P., Vasile, E., Acasandrei, A., Popescu, R. C., Savu, D. and Kusko, M. (2019) Comparative analysis of honey and citrate stabilized gold nano-particles: In vitro interaction with proteins and toxicity studies. *Journal of Photochemistry and Photobiology B: Biology*, **197**, 1–10.

33. Wang, S., Yao, H., Sato, S. and Kimura, K. (2004). Inclusion-water-cluster in a three-dimensional superlattice of gold nanoparticles. *Journal of the American Chemical Society*, **126 (24)**, 7438–7439.

34. Wulandari, P., Nagahiro, T., Fukada, N., Kimura, Y. and Niwano, M. (2015) Characterization of citrates on gold and silver nanoparticles. *Journal of Colloid and Interface Science*, **438**, 244–248.

35. Wulandari, P., Nagahiro, T., Michioka, K., Tamada, K., Ishibashi, K. Ichi, Kimura, Y. and Niwano, M. (2008) Coordination of carboxylate on metal nanoparticles characterized by Fourier transform infrared spectroscopy. *Chemistry Letters*, **37(8)**, 888–889.

36. Osman, M. J., Yunus Wan, W. M. Z., Ong, K. K., Chieng, B. W., Mohd Kassim, N. A., Mohd Noor, S. A., Knight, V. F., Abdul Rashid, J. I., and Teoh, C. C. (2020) Image digitization of colorimetric detection of acephate based on its complexation with citrate-capped gold nano-particles. *Journal of Chemistry*, **2020**, 1–10.

37. Jiang, W., Hibbert, D. B., Moran, G., Herrmann, J., Jamting, A. K. and Coleman, A. K. (2013) Characterisation of gold agglomerates: size distribution, shape and optical properties. *RSC Advances*, **3(20)**, 7367-7374.

38. Ghosh, S. K. and Pal, T. (2007) Interparticle coupling effect on the surface plasmon resonance of gold nanoparticles : from theory to applications. *Chemical Reviews*, **107(11)**, 4797–4862.

39. Amendola, V., Pilot, R., Frasconi, M., Maragò, O. M. and Iatì, M. A. (2017) Surface plasmon resonance in gold nanoparticles: A review. *Journal of Physics: Condensed Matter*, **29(20)**.

40. Kuiri, P. K. (2020) Control of ultraviolet surface plasmon absorption of al nanoparticles by changing particle size, shape, interaction, and medium dielectric constant. *Plasmonics*, **15**, 933–940.

41. Stiolica, A. T., Popescu, M., Bubulica, M. V., Oancea, C. N., Nicolicescu, C., Manda, C. V., Neamtu, J., Croitoru, O. (2017) Optimization of gold nanoparticles synthesis using design of experiments technique. *Revista de Chimie*, **68(7)**, 1518–1523.

42. Pojol, F. E., Yusuff, S.M., Ong, K. K., Abdul Rashid, J. I., Jamari, N. L. -A., Mohd Noor, S. A., Mohd Kasim, N. A., Abdul Halim, N. Wan Yunus, W. M. Z., Knight, V. F. and Teoh, C. C. (2020) Optimisation of colorimetric aptasensor for determination of methylphosphonic acid using response surface methodology. *Defence S & T Technical Bulletin*, **13(2)**, 188–195.

43. Chatterjee, S., Kumar, A., Basu, S. and Dutta, S. (2012) Application of response surface methodology for methylene blue dye removal from aqueous solution using low cost adsorbent. *Chemical Engineering Journal*, **181–182**, 289–299.

44. Sarkar, M. and Majumdar, P. (2011) Application of response surface methodology for optimization of heavy metal biosorption using surfactant modified chitosan bead. *Chemical Engineering Journal*, **175(1)**, 376–387.

45. Shakeel, F., Haq, N., Alanazi, F. K. and Alsarra, I. A. (2014) Box-Behnken statistical design for removal of methylene blue from aqueous solution using sodium dodecyl sulfate self-microemulsifying systems. *Industrial and Engineering Chemistry Research*, **53(3)**, 1179–1188.

46. Malakootian, M., Hamzeh, S. and Mahmoudi-Moghaddam, H. (2020) A new electrochemical sensor for simultaneous determination of Cd (II) and Pb (II) using FeNi3/CuS/BiOCl: RSM optimization. *Microchemical Journal*, **158(Ii)**, 105194.

47. Divsar, F., Habibzadeh, K., Shariati, S. and Shahriarinour, M. (2015) Aptamer conjugated silver nanoparticles for the colorimetric detection of arsenic ions using response surface methodology. *Analytical Methods*, **7(11)**, 4568–4576.

48. Plotnikov, E., Zhuravkov, S., Gapeyev, A., Plotnikov, V., Martemianova, I. and Martemianov, D. (2017) Comparative study of genotoxicity of silver and gold nanoparticles prepared by the electric spark dispersion method. *Journal of Applied Pharmaceutical Science*, **7(7)**, 035–039.

49. Wang, L., Wan, Y., Xu, Q. and Lou, X. (2019) Long-term functional stability of functional nucleic acid-gold nanoparticle conjugates with different secondary structures. *Langmuir*, **35(36)**, 11791–11798.

50. Pan, G., Chang, G., Chen, H. and Giusti, L. (2007) Assessment of the relative toxicity of Cu^{2+} by measuring structural changes of supercoiled DNA. *Environmental Pollution*, **148(2)**, 477–482.

51. Smith, J. E., Chávez, J. L., Hagen, J. A. and Kelley-Loughnane, N. (2016) Design and development of aptamer–gold nanoparticle based colorimetric assays for in-the-field applications. *Journal of Visualized Experiments*, **2016(112)**, 1–10.

52. May, S., Hirsch, C., Rippl, A., Bohmer, N., Kaiser, J. P., Diener, L., Wichser, A., Bürkle, A. and Wick, P. (2018) Transient DNA damage following exposure to gold nanoparticles. *Nanoscale*, **10(33)**, 15723–15735.

53. Verger, E., Cheng, J., de Santis, V., Iafrate, M., Jackson, J. A., Imberti, C., Fruhwirth, G. O., Blower, P. J., Ma, M. T., Burnham, D. R. and Terry, S. Y. A. (2021) Validation of the plasmid study to relate DNA damaging effects of radionuclides to those from external beam radiotherapy. *Nuclear Medicine and Biology*, **100–101**, 36–43.

54. Peng, H., Hui, Y., Ren, R., Wang, B., Song, S., He, Y. and Zhang, F. (2019) A sensitive electrochemical aptasensor based on MB-anchored GO for the rapid detection of *Cronobacter sakazakii*. *Journal of Solid State Electrochemistry*, **23(12)**, 3391–3398.